

First-principles insights into strain-mediated He migration and irradiation resistance in W-Ta-Cr-V complex alloys

Mengdie Wang(王梦蝶), Chao Zhang(张超), Xinyue Lan(兰新月), Biao Hu(胡标), and Xuebang Wu(吴学邦)
Citation: Chin. Phys. B, 2026, 35 (**1**): 016102. DOI: 10.1088/1674-1056/ae29fb
http://cpb.iphy.ac.cn; http://iopscience.iop.org/cpb

What follows is a list of articles you may be interested in

Site occupation of Al doping in Lu_2SiO_5: The role of ionic radius versus chemical valence

Xuejiao Sun(孙雪娇), Yu Cui(崔宇), Feng Gao(高峰), Zhongjun Xue(薛中军), Shuwen Zhao(赵书文), Dongzhou Ding(丁栋舟), Fan Yang(杨帆), and Yi-Yang Sun(孙宜阳)
Chin. Phys. B, 2025, 34 (**9**): 096101. DOI: 10.1088/1674-1056/add678

Hyperparameter optimization and force error correction of neuroevolution potential for predicting thermal conductivity of wurtzite GaN

Zhuo Chen(陈卓), Yuejin Yuan(袁越锦), Wenyang Ding(丁文扬), Shouhang Li(李寿航), Meng An(安盟), and Gang Zhang(张刚)
Chin. Phys. B, 2025, 34 (**8**): 086110. DOI: 10.1088/1674-1056/add905

Evolution of helium bubbles in nickel-based alloy by post-implantation annealing

Rui Zhu(朱睿), Qin Zhou(周钦), Li Shi(史力), Li-Bin Sun(孙立斌), Xin-Xin Wu(吴莘馨), Sha-Sha Lv(吕沙沙), and Zheng-Cao Li(李正操)
Chin. Phys. B, 2021, 30 (**8**): 086102. DOI: 10.1088/1674-1056/ac0783

Comparison of helium bubble formation in F82H, ODS, SIMP and T91 steels irradiated by Fe and He ions simultaneously

Bingsheng Li(李炳生), Zhen Yang(杨振), Shuai Xu(徐帅), Kongfang Wei (魏孔芳), Zhiguang Wang(王志光), Tielong Shen(申铁龙), Tongmin Zhang(张桐民), and Qing Liao(廖庆)
Chin. Phys. B, 2021, 30 (**3**): 036102. DOI: 10.1088/1674-1056/abc2b4

Effects of helium irradiation dose and temperature on the damage evolution of Ti_3SiC_2 ceramic

Hua-Hai Shen(申华海), Xia Xiang(向霞), Hai-Bin Zhang(张海斌), Xiao-Song Zhou(周晓松), Hong-Xiang Deng(邓洪祥), Xiao-Tao Zu(祖小涛)
Chin. Phys. B, 2019, 28 (**7**): 076104. DOI: 10.1088/1674-1056/28/7/076104

First-principles insights into strain-mediated He migration and irradiation resistance in W–Ta–Cr–V complex alloys

Mengdie Wang(王梦蝶)[1], Chao Zhang(张超)[1,†], Xinyue Lan(兰新月)[1], Biao Hu(胡标)[1], and Xuebang Wu(吴学邦)[2,‡]

[1] *School of Materials Science and Engineering, Anhui University of Science and Technology, Huainan* 232001, *China*
[2] *Key Laboratory of Materials Physics, Institute of Solid State Physics, HFIPS, Chinese Academy of Sciences, Hefei* 230031, *China*

(Received 8 September 2025; revised manuscript received 4 December 2025; accepted manuscript online 9 December 2025)

High-performance intelligent protective materials are vital for nuclear energy systems exposed to extreme irradiation. Among them, tungsten-based alloys demonstrate exceptional potential owing to their superior irradiation resistance. Recent experimental studies have demonstrated that W–Ta–Cr–V alloys exhibit excellent irradiation resistance under helium (He) ion irradiation. However, the underlying mechanisms, especially the migration behavior of He atoms, remain unclear. In this work, the influences of uniaxial tensile and compressive strain on He migration in W–Ta–Cr–V complex alloys have been systematically studied through first-principles calculations. Our results demonstrate that He atoms preferentially occupy the tetrahedral interstitial sites, with interstitial formation energies significantly reduced compared to pure W. The introduction of Ta, Cr, and V alloying elements markedly increases the He migration barriers, effectively suppressing He diffusion. Compressive strain increases the migration barriers, inhibiting He bubbles nucleation and growth, while tensile strain decreases the barriers, facilitating bubble formation. Compared to pure W, the W–Ta–Cr–V alloys exhibit both lower He interstitial formation energies and higher migration barriers, with further enhancement under compressive strain. Specifically, compressive strain of 6% increases the He migration barrier of the W–Ta–Cr–V alloy by 0.166 eV, which further widens the difference relative to pure W. These findings provide a theoretical explanation for the superior irradiation resistance of tungsten-based alloys observed experimentally and promote the understanding of irradiation damage in these alloys under strain.

Keywords: He bubbles, migration barriers, tensile/compressive strain, W–Ta–Cr–V alloys, first-principles calculations

PACS: 61.72.–y, 66.30.–h, 62.20.–x, 61.66.Dk, 71.15.–m

DOI: 10.1088/1674-1056/ae29fb **CSTR:** 32038.14.CPB.ae29fb

1. Introduction

The structural materials of nuclear reactors, particularly the fuel cladding, are subjected to extreme conditions during service, including high-flux neutron irradiation, high-temperature oxidation, aggressive corrosion, and multi-physical coupling stresses. Under such harsh conditions, the materials inevitably undergo microstructural changes, such as the accumulation of irradiation defects and phase transformation, which leads to macroscopic performance degradation and affects the service life and operation safety of reactors.[1–4] Notably, high-reliability and high-performance intelligent protective materials for such extreme environment applications are among the current frontiers in materials research — particularly in advanced nuclear energy systems involving high-energy particle irradiation, where the design and mechanism study of new irradiation-resistant structural materials are of great significance.[5] This demand becomes more urgent as the service environment in the fourth-generation nuclear power systems is even more severe, with an order-of-magnitude increase in irradiation dose, higher temperature gradient, and more complex stress conditions, making the damage to structural materials exacerbated.[6–9] Currently, irradiation-induced material degradation has become a main bottleneck restricting the development of the next-generation nuclear energy systems. Consequently, substantial scientific efforts have been devoted to investigating the irradiation damage of candidate structural materials, aiming to develop irradiation-resistant materials for advanced nuclear applications.[10–14]

Tungsten (W) is regarded as a promising plasma-facing material (PFM) for next-generation fusion reactors owing to its exceptional combination of properties, including an extremely high melting temperature, excellent thermal conductivity, reduced erosion from sputtering effects, and suppressed tritium retention.[15–19] However, despite these favorable characteristics, pure W is inherently brittle with poor ductility at ambient temperatures and has an elevated ductile-to-brittle transition temperature.[20,21] These limitations are further aggravated by significant irradiation-induced hardening and embrittlement, particularly the formation of nanoscale He bubbles and low-density porous structures under irradiation,[22] limiting the practical application of pure W in extreme fusion environments.[23] To overcome these challenges, re-

†Corresponding author. E-mail: chaozhang@mail.bnu.edu.cn
‡Corresponding author. E-mail: xbwu@issp.ac.cn

© 2026 Chinese Physical Society and IOP Publishing Ltd. All rights, including for text and data mining, AI training, and similar technologies, are reserved.

searchers have developed several modification strategies, such as the addition of minor dopant elements,[24] microstructure regulation,[25] preparation process optimization,[26,27] and surface modification treatments.[28]

Recent studies have demonstrated that W-based high-entropy alloys (HEAs) exhibit superior mechanical behaviors and enhanced irradiation resistance.[29–32] First-principles calculations by Qin *et al.* revealed that the addition of Ta and V significantly enhances the ductility of pure W, and the B/G ratio (Pugh's ratio) of W–Ta–Cr–V alloy exceeds 1.75, effectively reducing the intrinsic brittleness of W.[29] Kalita *et al.* observed the formation of uniformly dispersed nanoscale He bubbles in equimolar W–Ta–Cr–V HEAs irradiated with 200 keV He ions, with no dislocation loops or significant irradiation hardening observed.[30] Similarly, El-Atwani *et al.* reported comparable irradiation tolerance in non-equimolar $W_{38}Ta_{36}Cr_{15}V_{11}$ HEAs. After irradiation with 1 MeV Kr^{2+} ions up to 8 dpa, no irradiation-induced dislocation loop was observed.[31] Additionally, Shi *et al.* demonstrated that W–Ta–Cr–V complex concentrated alloys (CCAs) exhibit smaller He bubbles with shallower distributions compared to pure W under the irradiation of He plasma with 100 eV (2.02×10^{25} He/m^2).[32] While these findings highlight the superior irradiation resistance of W-based complex alloys, the mechanisms of irradiation damage, particularly the migration behavior of He in W–Ta–Cr–V alloys and the role of local atomic environments, remain unclear.

In practical service environments, W-based alloys are exposed not only to neutron irradiation but also to complex external stress, including tensile/compressive and thermal stresses. These stress fields exert a significant influence on the He atom migration, the He cluster formation, and the subsequent nucleation and growth of He bubbles. Notably, additional stress can alter the preferential occupation sites of He atoms and modify their migration pathways.[33] Therefore, it is crucial to investigate the effect of stress on the He atom migration in W-based complex alloys to elucidate the underlying mechanisms of irradiation-induced damage.

In this work, the influences of both tensile and compressive stresses on the He migration behavior in W–Ta–Cr–V complex alloys were systematically investigated through first-principles calculations. A comprehensive examination of He interstitial occupation, diffusion mechanisms, strain-dependent effects, and correlations with local chemical environment was presented by comparative analyses of He atom behavior in pure W. These results not only fill a critical knowledge gap regarding external stress effects on the migration behavior of He atoms, but also provide valuable theoretical insights into mechanisms of irradiation damage in W-based alloys.

2. Methodology

2.1. DFT calculation details

All calculations were performed by first-principles calculations based on density functional theory (DFT), as implemented in the Vienna *Ab initio* Simulation Package (VASP).[34,35] The exchange–correlation interactions were described by the Perdew–Burke–Ernzerhof (PBE) generalized gradient approximation (GGA),[36,37] and the electron–ion interactions were modeled with projector augmented-wave (PAW) pseudopotentials. A plane-wave cutoff energy of 400 eV was employed, with convergence thresholds of 0.02 eV/Å and 10^{-5} eV for Hellmann–Feynman forces and electronic self-consistent energy during geometric optimization. For the $4 \times 4 \times 2$ supercells ($W_{48}Ta_4Cr_8V_4$ alloy), Brillouin zone integration employed a Γ-centered $3 \times 3 \times 5$ grid to ensure equivalent k-point sampling density. This specific composition was selected as it lies within the BCC solid-solution region of the W–Ta–Cr–V system, thereby capturing the characteristic chemical disorder and lattice distortion of these complex alloys. Moreover, the atomic ratio enables a relatively uniform distribution of alloying elements, facilitating effective sampling of diverse local chemical environments within the finite supercell. Following the above parameter standards, the tungsten lattice constant was computed as 3.165 Å, which shows good agreement with the experimental value (3.164 Å),[38] thereby verifying the reliability of the calculation method. The schematic diagram for the crystal structure of the W–Ta–Cr–V complex alloy is displayed in Fig. 1(a).

2.2. He interstitial sites and local chemical environment

First-principles calculations identified three primary trapping sites for isolated He atoms in pristine tungsten lattices, namely substitutional (Sub), tetrahedral interstitial (Tetra), and octahedral interstitial (Octa) sites.[39] Although previous studies have shown that the lowest energy site for a He atom in pure W is the Sub site,[40] a He atom usually starts at the interstitial site and then migrates until it occupies a vacancy. Therefore, the interstitial site serves a vital function in facilitating He migration to Sub sites. Moreover, He atoms tend to aggregate into clusters or bubbles in metals, and the formation of these clusters often begins with the migration and aggregation of He interstitial atoms. Given the significantly smaller atomic radius of He compared to W, Ta, Cr, and V atoms, the present study primarily investigates their interstitial migration behavior as the dominant diffusion mechanism for He in the alloys.[41–43]

This work focuses on the influence of the local chemical environment of W–Ta–Cr–V alloys on the formation energy and migration energy of He interstitial atoms. Therefore, multiple atomic configurations of helium atoms were considered, as shown in Figs. 1 and S1. To ensure statistical significance

and comprehensively capture the chemical disorder, we systematically identified all geometrically distinct tetrahedral and octahedral interstitial sites in the $4 \times 4 \times 2$ supercell. The local chemical environment of each site was analyzed based on the species and arrangement of atoms within its first coordination shell to define its uniqueness. This procedure identified exactly 73 distinct initial He configurations, each possessing a unique local chemical environment. The ground-state configuration was determined by systematically comparing the formation energies of all candidate structures after full geometry optimization at the DFT level, with ionic relaxations conducted until the forces on each atom converged below 0.02 eV/Å. The structure exhibiting the minimal formation energy was subsequently chosen for further analysis, as it represents the most thermodynamically stable configuration under equilibrium conditions.[41] This configuration served as the reference state for investigating strain effects on helium behavior, particularly in determining formation energies under applied tensile/compressive strains and evaluating migration energy barriers through systematic first-principles calculations.

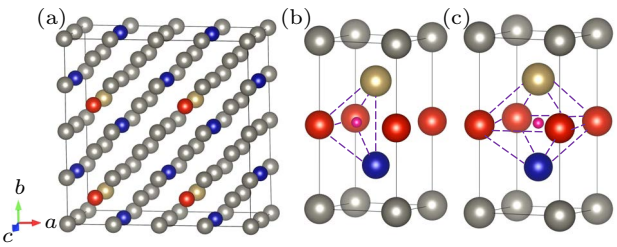


Fig. 1. (a) The schematic diagram for crystal structure of W–Ta–Cr–V complex alloy. (b) Tetrahedral (Tetra) and (c) octahedral (Octa) interstitial sites in body-centered cubic (BCC) crystal lattices. Distinct atomic elements are color-coded as follows: tungsten (W, gray), tantalum (Ta, yellow), chromium (Cr, blue), vanadium (V, red), and helium (He, pink).

2.3. Strain application and migration path calculation

To study the He migration behavior and stress effects, both the W–Ta–Cr–V alloy and pure W systems were modeled using $4 \times 4 \times 2$ supercells with identical dimensions. The He migration pathways were determined using the climbing image-nudged elastic band (CI-NEB) method,[44] with convergence thresholds of 10^{-5} eV for total energy and 0.03 eV/Å for atomic forces during transition state searches. Importantly, the initial and final tetrahedral sites for He migration shared identical local atomic environments (i.e., equivalent spatial distributions of W, Ta, Cr, and V atoms around the interstitial sites), ensuring that the calculated energy barriers solely reflect the intrinsic migration process without interference from environmental variations. Uniaxial strains ranging from -6% to $+6\%$ were applied along the c-axis ([001] direction) to systematically evaluate strain effects. This range was selected to achieve three objectives: to cover typical elastic strain levels under service conditions, to ensure a physically meaningful lattice response, and to maintain direct comparability with the pure W study,[41] thereby isolating intrinsic alloying effects. Periodic boundary conditions were maintained in all three crystallographic directions (a, b, and c). The c-axis was selected for detailed presentation because preliminary calculations on all three principal axes indicated that it yielded the clearest and most representative trends.

2.4. Formation energy calculation

The formation energy of interstitial He atoms ($E^{\mathrm{f}}_{\mathrm{He}}$) was computed via the equation[45]

$$E^{\mathrm{f}}_{\mathrm{He}} = E_{\mathrm{supercell+He}} - E_{\mathrm{supercell}} - \mu_{\mathrm{He}} - \sum_{i=\mathrm{W,Ta,Cr,V}} n_i \Delta\mu_i, \quad (1)$$

where $E_{\mathrm{supercell+He}}$ and $E_{\mathrm{supercell}}$ are the total energies of the alloy supercell with and without He interstitial, respectively. μ_{He} is the chemical potential of He, calculated as the energy of an isolated He atom in a 10 Å cubic box. n_i represents the number of alloying elements involved in the defect process, and for a pure interstitial defect like the case studied here, $n_i = 0$, thus the term $\sum_{i=\mathrm{W,Ta,Cr,V}} n_i \Delta\mu_i$ vanishes. $\Delta\mu_i$ accounts for the chemical potential difference of element i between the alloy and its pure bulk phase. Lower formation energies indicate that the He point defects are more likely to form in the alloys.

By calculating the He formation energies at Tetra and Octa sites in W, it was found that the formation energy at the Tetra site (6.44 eV) is lower than that at the Octa site (6.74 eV). The energy difference between the two sites is 0.30 eV, which indicates that He atom exhibits a stronger preference for the Tetra site. The results show remarkable consistency with prior investigations reported by Yang *et al.*,[46] Zhou *et al.*[41] and Becquart *et al.*,[47] confirming the correctness of the model and the method used in this work.

3. Results

3.1. Formation energy of He interstitial atom

Figures 2(a) and 2(b) exhibit the formation energies distribution of He in Tetra and Octa interstitial sites in W–Ta–Cr–V alloys, respectively. It is observed that He interstitial formation energies in W–Ta–Cr–V alloys are substantially reduced compared to pure W, while maintaining the same site preference where tetrahedral positions remain energetically favorable. However, the site preference in W–Ta–Cr–V alloys is less pronounced compared to pure W, which can be attributed to the reduced symmetry caused by lattice distortion.[45] This is confirmed by the smaller difference in the average formation energy at Tetra sites (4.9 eV) and that at Octa sites (5.1 eV). In addition, the formation energies of He atoms in W–Ta–Cr–V alloys show stronger local dependence, with a significantly wider distribution range. This indicates that the stability of He atoms is highly sensitive to the local chemical environment.

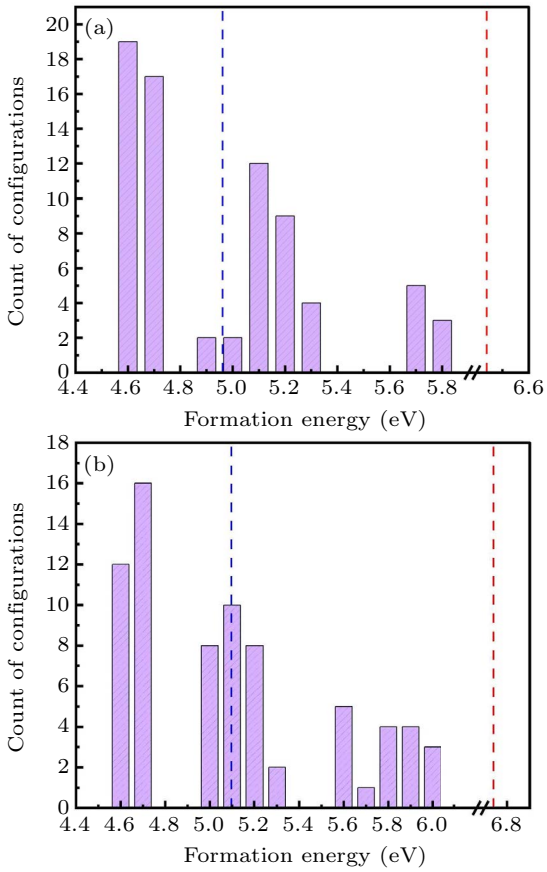


Fig. 2. Formation energy distribution of a single He interstitial atom in W–Ta–Cr–V alloys: (a) Tetra site and (b) Octa site. The red dashed lines in panels (a) and (b) denote the formation energies of He interstitial atoms in pure W. The blue dashed lines in panels (a) and (b) show the average He interstitial formation energies in W–Ta–Cr–V alloys.

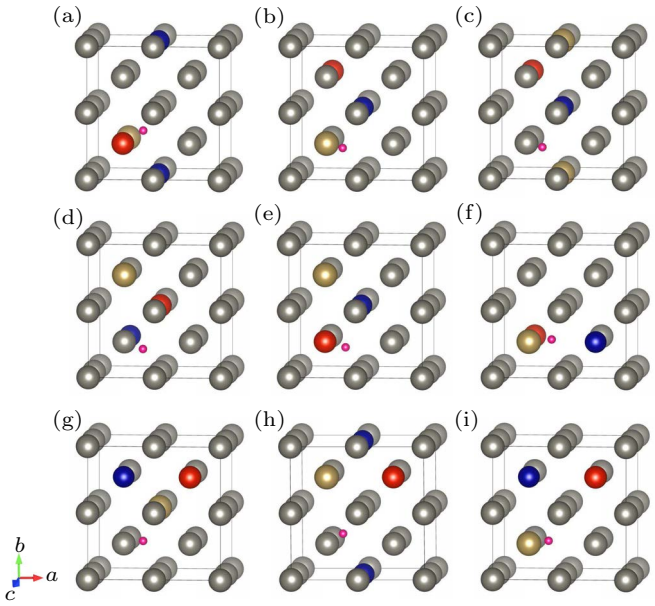


Fig. 3. Structures of W–Ta–Cr–V alloys corresponding to different He interstitial formation energies in Fig. 2: (a) 4.6 eV, (b) 4.7 eV, (c) 4.9 eV, (d) 5.0 eV, (e) 5.1 eV, (f) 5.2 eV, (g) 5.3 eV, (h) 5.7 eV, and (i) 5.8 eV. The W, Ta, Cr, V, and He atoms are represented by gray, yellow, blue, red, and tiny pink spheres, respectively.

Figure 3 shows representative atomic configurations of W–Ta–Cr–V alloy corresponding to the Tetra interstitial He formation energies shown in Fig. 2. Among the 73 calculated configurations, only one typical structure is presented for structures with the same formation energy. The structures demonstrate the diversities of local chemical environments in the W–Ta–Cr–V alloys, where significant variations are observed in the He-occupied Tetra sites across different atomic arrangements. A quantitative analysis of the local chemical environments (Table S1) and the final He positions (Table S2) reveals a clear structure–property relationship. The stability of the He interstitial is governed by a combination of local atomic size mismatch and chemical bonding effects. For instance, the configuration with the lowest formation energy (4.6 eV, Fig. 3(a)) is surrounded by a mix of large (Ta), medium (W, V), and small (Cr) atoms. This significant size variation creates a highly distorted lattice that accommodates the He atom more easily, lowering the formation energy. Concurrently, alloying elements with electronic properties distinct from W (e.g., Ta) modify the local charge distribution, potentially weakening He-host repulsion. In contrast, a high formation energy configuration (5.8 eV, Fig. 3(i)) is coordinated predominantly by W atoms, resulting in a uniform, rigid environment with less inherent distortion. This rigidity increases the energy cost of accommodating He, leading to stronger repulsion. It indicates that the alloying elements (Ta, Cr, V) exert varying effects on the formation energies of He atoms, arising from the pronounced chemical disorder induced by differences in atomic radii and electronic structures among Ta, Cr, and V atoms. Because the average formation energy of He atoms at the Tetra sites in W–Ta–Cr–V alloys is lower than that at the Octa sites, the following work is carried out for the Tetra site to examine strain effects on the formation energies of He atoms, and focused on the W–Ta–Cr–V alloy structure with the lowest formation energy of He atoms at the Tetra sites (see Figs. 2(a) and 3(a)). Figure 4 presents the effect of strain on the Tetra He formation energies in the W–Ta–Cr–V alloys. It is observed that the

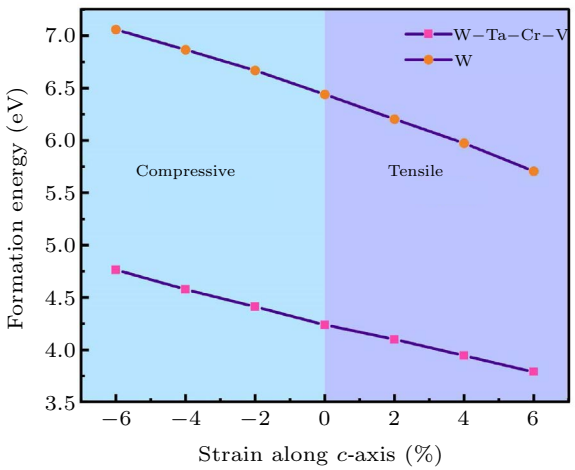


Fig. 4. Strain dependence of the formation energies for helium interstitial atoms.

formation energy rises with increasing compressive strain and falls with increasing tensile strain. The phenomenon can be explained by the lattice shrinkage and changes in the atomic interaction distance. Under uniaxial compressive strain along the *c*-axis, the W–Ta–Cr–V alloy undergoes lattice contraction in the *c*-axis direction, with a decrease in the atomic spacing. At the same time, the atomic spacing increases in the *a*- and *b*-axis directions due to the Poisson effect,[48] leading to lattice expansion along the direction normal to the *c*-axis. As shown in Fig. 5(a), under 6% compressive strain along the *c*-axis, the distances between the nearest-neighbor atoms around the He interstitial atom increase to 3.268 Å along the *a*-axis and 3.403 Å along the *b*-axis, compared with the unstrained state (see Fig. 5(b)). Furthermore, electron density analysis reveals that the overlap of electron clouds between He and its surrounding atoms increases under the 6% compressive strain (see Fig. 6(a)). This enhanced overlap directly strengthens the repulsive force between He and surrounding atoms. Specifically, greater electron cloud overlap leads to a higher concentration of negative charge in the overlapping region, which in turn amplifies this repulsive interaction. Conversely, reduced overlap would lower the negative charge concentration in the overlapping area, thereby weakening the repulsion. This increased repulsion further causes a rise in the energy barrier at the Tetra site, ultimately increasing the formation energy of He interstitial atoms.

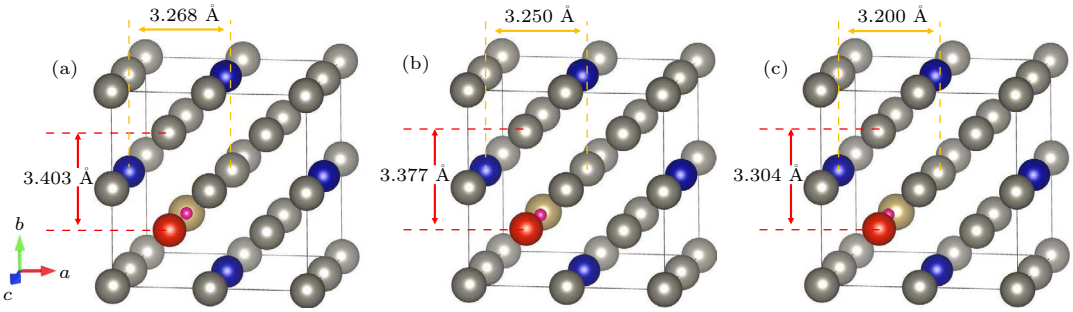


Fig. 5. Evolution of the nearest-neighbor atomic spacing around the He interstitial atoms in the W–Ta–Cr–V alloy under (a) compressive strain (−6%), (b) no strain (0%), and (c) tensile strain (6%). The W, Ta, Cr, V, and He atoms are represented by gray, yellow, blue, red, and tiny pink spheres, respectively. For clarity, the figure shows only the relevant local atomic environment around He interstitials, and does not display the full $4 \times 4 \times 2$ supercell.

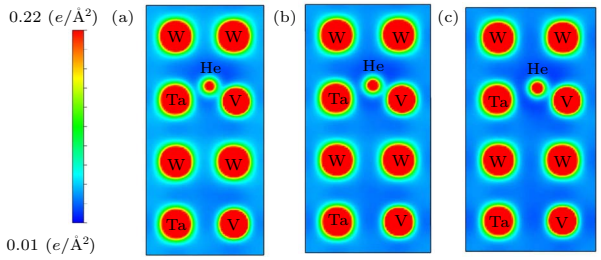


Fig. 6. Variation of the charge density under (a) compressive strain (−6%), (b) no strain (0%), and (c) tensile strain (6%). The contour values represent the magnitude of charge density, with higher values indicating more significant electron cloud overlap. The smaller circles represent the He interstitial atoms. For clarity, the figure shows only the relevant local atomic environment around He interstitials, and does not display the full $4 \times 4 \times 2$ supercell.

When the tensile strain is applied along the *c*-axis, the lattice expands in the *c*-axis direction, which increases atomic spacing. However, the spacing decreases along the *a*-axis and *b*-axis, resulting in lattice contraction perpendicular to the tensile direction. As depicted in Fig. 5(c), after applying 6% tensile strain along the *c*-axis direction, the distances between the two nearest-neighbor atoms around the He interstitial atom shorten to 3.200 Å in the *a*-axis direction and 3.304 Å in the *b*-axis direction, compared with the unstrained state (see Fig. 5(b)). Moreover, the electron density analysis indicates a significant decrease in overlap between He and surrounding atoms under the 6% tensile strain (see Fig. 6(c)), which leads to a weakening of the repulsive force between atoms and a decrease in the energy barrier for forming the He interstitial. The finding indicates that the tensile strain promotes the formation of He interstitial atoms. Furthermore, the He interstitial formation energies in W–Ta–Cr–V alloy under strain are lower than those in pure W. This phenomenon is mainly attributed to the multi-component nature, chemical disorder, and local lattice distortions in the W–Ta–Cr–V alloy,[49,50] which make it more prone to He interstitial formation under strain conditions.

3.2. Migration behavior of He interstitial atoms

Now, we focus on the migration behavior of He interstitial atoms based on the structure with the minimum formation energy at the Tetra site in the W–Ta–Cr–V alloy (see Fig. 3(a)). Figure 7 shows the migration energy barriers for helium atoms in pure W and W–Ta–Cr–V alloys calculated by CI-NEB without the application of external strain. The results show that the migration energy for a He interstitial atom from the initial to the final states at tetrahedral sites in pure W is 0.080 eV, which agrees well with the value of 0.081 eV reported by Gonzalez *et al.*[51] In the W–Ta–Cr–V alloy, the migration barrier is 0.379 eV, which is 0.299 eV higher than that in pure W. Figure 8 shows the strain dependence of migration energies in the W–Ta–Cr–V alloy. It can be observed that the energy barrier for atomic migration exhibits a monotonic increase with ap-

plied compressive strain, while tensile strain reduces the migration energy. A similar trend is observed in pure W.

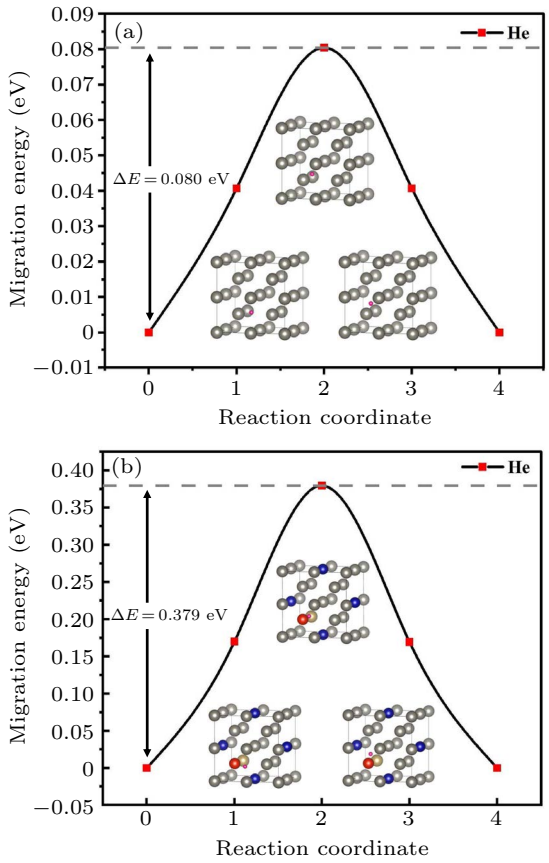


Fig. 7. Migration energy barriers of He interstitial atoms in (a) pure W and (b) W–Ta–Cr–V alloy. For clarity, the figure shows only the relevant local atomic environment around He interstitials, and does not display the full $4 \times 4 \times 2$ supercell.

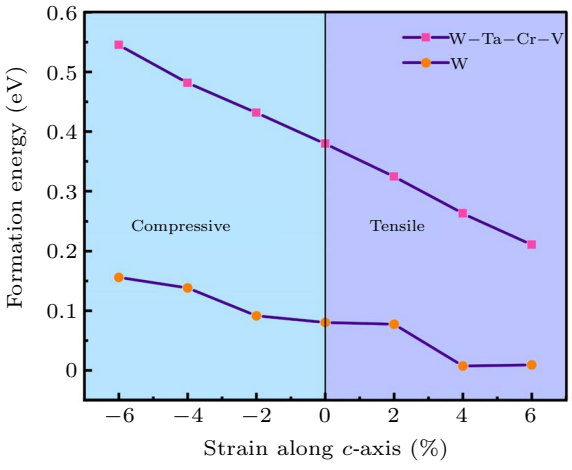


Fig. 8. Strain dependence of He interstitial migration energy.

4. Discussion

Through first-principles calculations, we have comprehensively studied the formation energies and migration behaviors of He interstitial atoms in W–Ta–Cr–V alloys under different strain conditions, and made detailed comparisons with the pure W. Our results reveal distinct variations in He interstitial stability, site preference, and strain response between the two materials, particularly highlighting the crucial role of alloying-induced lattice distortion and chemical disorder in altering He behavior. These distinct features originate from the local atomic environments and strain-modulated electronic interactions, which will be thoroughly analyzed in terms of their underlying mechanisms and implications for irradiation resistance.

4.1. Alloying and strain effects on He migration behavior

The migration barrier of He interstitial atoms in W–Ta–Cr–V alloy is 0.379 eV, significantly higher than that (0.080 eV) of pure W (see Fig. 7). This difference is mainly ascribed to the local lattice distortion and electronic structure changes caused by the incorporation of Ta, Cr, and V elements. The presence of these alloying elements not only enhances the lattice distortion but also redistributes the electron cloud through charge transfer effects (e.g., electronegativity differences), thereby significantly increasing the energy barrier for the migration of He atoms.[52] These findings suggest that the incorporation of alloying elements changes the local chemical environment, affecting He migration behavior. Moreover, the migration path length of a He interstitial atom in the W–Ta–Cr–V alloy from the initial state to the final state is 1.636 Å (see Fig. 9(b)), compared to just 1.093 Å in pure W (see Fig. 9(e)). Therefore, the introduction of alloying elements not only increases the migration barrier, but also elongates the migration path of the He interstitial atom. This serves to inhibit the diffusion and aggregation of He atoms, thereby enhancing the irradiation resistance of W–Ta–Cr–V alloys to He ion irradiation. Our computational results are consistent with the experimental phenomena reported by Wang *et al.*[53] In their study of an irradiated W–Ta–Cr–V alloy, they reported a prominent non-directional distribution of much smaller helium bubbles, contrasting the large, orderly-aligned bubbles typically found in pure W. Our results thus identify suppressed helium diffusion as the underlying atomistic mechanism responsible for this superior performance.

As illustrated in Fig. 8, the strain-induced migration energy changes result from a significant reconstruction of the local environment around the tetrahedral interstitial sites. Specifically, the migration path length of He interstitial atoms perpendicular to the *c*-axis increases from 1.636 Å to 1.757 Å under compressive strain (see Figs. 9(a) and 9(b)). Conversely, tensile strain along the *c*-axis leads to a reduction in the migration path length from 1.636 Å to 1.549 Å (see Figs. 9(b) and 9(c)). The pure W system exhibits similar migration behavior of He atoms under strain, as shown in Figs. 9(d)–9(f). Under compressive and tensile strains, the migration path lengths of He atoms in pure W range from 1.093 Å to 1.289 Å, and from 1.093 Å to 0.821 Å, respectively.

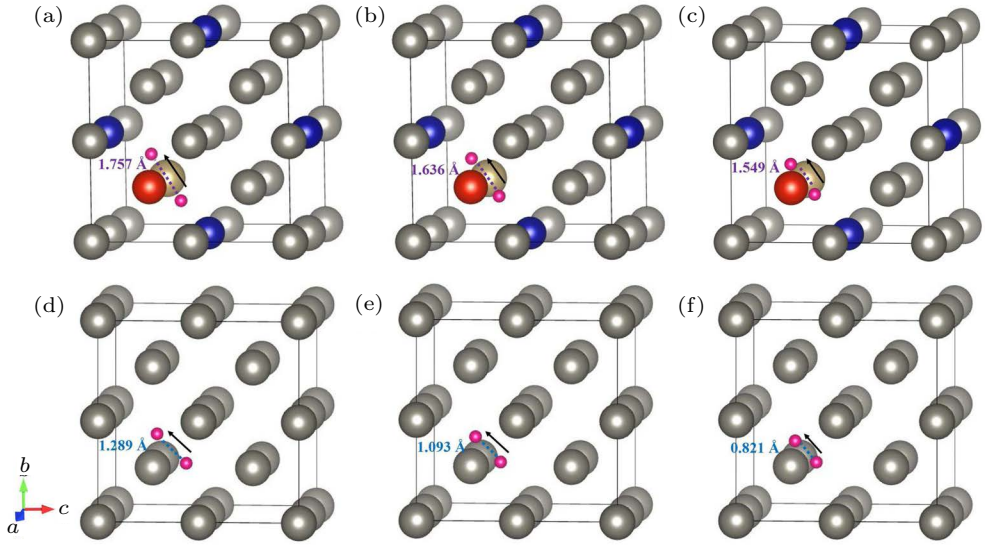


Fig. 9. Migration paths of He interstitial atoms in the W–Ta–Cr–V alloy (a)–(c) and pure W (d)–(f) under −6%, 0%, and 6% strains. For clarity, the figure shows only the relevant local atomic environment around He interstitials, and does not display the full $4 \times 4 \times 2$ supercell.

4.2. Strain-modulated charge density distributions

Figure 10 shows the charge density distributions of the transition state structures for He atom migration in the W–Ta–Cr–V alloy under three strain states of −6%, 0%, and 6%. It is observed that compression along the *c*-axis leads to a significant increase in the overlap region of the electron cloud between He and the surrounding atoms compared to the unstrained case (see Figs. 10(a) and 10(b)), which results in a stronger repulsive interaction between atoms. In contrast, the tensile strain reduces the overlap region of the electron cloud, as shown in Fig. 10(c), thereby weakening the repulsive interaction.

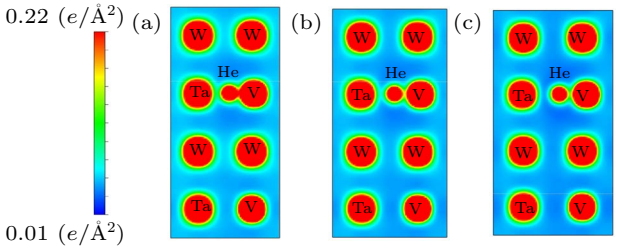


Fig. 10. Charge density distribution of the transition state structure under (a) compressive strain (−6%), (b) no strain (0%), and (c) tensile strain (6%). The contour values represent the magnitude of charge density, with higher values indicating more significant electron cloud overlap. The smaller circles represent the He interstitial atoms. For clarity, the figure shows only the relevant local atomic environment around He interstitials, and does not display the full $4 \times 4 \times 2$ supercell.

The strain-induced changes in geometric structure and electron cloud distribution elucidate the mechanism of variation in the He migration barrier. Specifically, the compressive strain elevates the migration barrier by increasing the migration path length and enhancing the repulsive interaction, while the tensile strain diminishes the migration barrier by reducing the migration path length and weakening the repulsive interaction. The aforementioned results suggest that the migration behavior of He interstitial atoms can be effectively regulated by applying external stresses. Thus, the compressive strain can inhibit He interstitial diffusion and delay the nucleation and growth of He bubbles, significantly enhancing the irradiation resistance of the W–Ta–Cr–V alloy, while the tensile strain can promote the migration of He interstitial atoms and accelerate the formation of He bubbles. Notably, the strain modulation effect is more pronounced in W–Ta–Cr–V alloys than in pure W, primarily due to the effect of local lattice distortions introduced by the alloying elements, which affects the migration behavior of He interstitial atoms.

5. Conclusion

This study employs first-principles calculations to systematically investigate how uniaxial tensile and compressive strains affect He atom migration in W–Ta–Cr–V alloys. The results show that the Tetra sites in W–Ta–Cr–V alloys are the preferential occupation sites for He atoms. The formation energies of the He interstitial atoms in W–Ta–Cr–V alloys are significantly lower than those in pure W. The introduction of alloying elements increases the migration barrier for He interstitials in W–Ta–Cr–V alloys compared to pure W. Strain significantly influences He migration behavior. The compressive strain enhances the He migration barrier and inhibits the diffusion of He interstitials, thereby hindering the nucleation and growth of He bubbles. Conversely, the tensile strain significantly reduces the He migration barrier and promotes He diffusion, thus accelerating the nucleation and growth of He bubbles.

The above findings demonstrate that the He migration behavior can be effectively modulated by applying external strains, directly modifying He bubble nucleation and growth. The increased migration barrier in W–Ta–Cr–V alloys

suggests superior irradiation resistance. Under compressive strains, the formation of He bubbles is mitigated, enhancing the irradiation resistance of the alloys. In contrast, pure W is more prone to form He bubbles due to the lower He migration barrier, leading to poorer irradiation resistance. These results not only provide critical theoretical guidance for the application of W–Ta–Cr–V high-entropy alloys in extreme conditions (e.g., advanced nuclear energy systems) via strain-regulated He migration, but also offer a critical theoretical basis and a composition-strain synergistic design strategy for developing new high-performance irradiation-resistant intelligent protective materials.

Acknowledgments

Project supported by the National Natural Science Foundation of China (Grant Nos. 11505003 and 52325103) and the Anhui Provincial Natural Science Foundation (Grant No. 2108085MA25).

References

[1] Was G S, Petti D, Ukai S and Zinkle S 2019 *J. Nucl. Mater.* **527** 151837
[2] Sun T Y, Niu T J, Shang Z X, Chen W Y, Li M M, Wang H Y and Zhang X H 2023 *Acta Mater.* **245** 118613
[3] Emerson J N, Marrero-Jackson E H, Nemets G A, Okuniewski M A and Wharry J P 2024 *Mater. Des.* **244** 113134
[4] Odette G R, Almirall N, Wells P B and Yamamoto T 2021 *Acta Mater.* **212** 116922
[5] Ouyang W H, Liu J B, Lai W S, Li J H and Liu B X 2023 *Chin. Phys. B* **32** 036101
[6] Fan C C, Li Q, Ding J, Liang Y X, Shang Z X, Li J, Su R Z, Cho J, Chen D, Wang Y Q, Wang J, Wang H Y and Zhang X H 2019 *Acta Mater.* **177** 107
[7] Zhang Y X, Schwen D, Zhang Y F and Bai X M 2019 *J. Alloys Compd.* **794** 482
[8] Náfrái G, Horváth E, Kollár M, Horváth A, Andricevic P, Sienkiewicz A, Forró L and Náfrádi B 2020 *Energy Convers. Manag.* **205** 112423
[9] Schmidt F, Hosemann P, Scarlat R O, Schreiber D K, Scully J R and Uberuaga B P 2021 *Annu. Rev. Mater. Res.* **51** 293
[10] Daghbouj N, Sen H S, Callisti M, Vronka M, Karlik M, Duchon J, Cech J, Havránek and Polcar T 2022 *Acta Mater.* **229** 117807
[11] Kalita P, Parveen R, Ghosh S, Grover V, Mishra Y K and Avasthi D K 2025 *J. Alloys Compd.* **1012** 178330
[12] Zinkle S J, Terrani K A, Gehin J C, Ott L J and Snead L L 2014 *J. Nucl. Mater.* **448** 374
[13] Reali L and Dudarev S L 2024 *Nucl. Fusion* **64** 056001
[14] Han W Z, Demkowicz M J, Mara N A, Fu E G, Sinha S, Rollett A D, Wang Y Q, Carpenter J S, Beyerlein I J and Misra A 2013 *Adv. Mater.* **25** 6975
[15] Linke J, Du J, Loewenhoff T, Pintsuk G, Spilker B, Steudel I and Wirtz M 2019 *Matter Radiat. Extrem.* **4** 056201
[16] Tan X Y, Luo L M, Lu Z L, Luo G N, Zan X, Zan J G and Wu Y C 2015 *Powder Technol.* **269** 437
[17] Tweer J, Day R, Derra T, Dorow-Gerspach D, Loewenhoff T, Wirtz M, Linsmeier C, Bergs T and Natour G 2024 *Nucl. Mater. Energy* **38** 101577
[18] Catarino N, Dias M, Lopes J, Jepu I and Alves E 2018 *Surf. Coat. Technol.* **355** 143
[19] Huang H X, Li Y H, Li Z Z, Hou P W, Ma F F, Ren Q Y, Zhou H B and Lu G H 2022 *Tungsten* **4** 219
[20] Pan S H, Yao G C, Cui Y N, Meng F S, Luo C, Zheng T Q and Singh G 2023 *Tungsten* **5** 1
[21] Liu L X, Jiang M X, Gao N, Chen Y C, Hu W Y and Deng H Q 2025 *Chin. Phys. B* **34** 046103
[22] Marian J, Becquart C S, Domain C, Dudarev S L, Gilbert M R, Kurtz R J, Mason D R, Nordlund K, Sand A E, Snead L L, Suzudo T and Wirth B D 2017 *Nucl. Fusion* **57** 092008
[23] Osetsky Y N 2021 *Tungsten* **3** 65
[24] Akopov G, Hu S L, Shumilov K D, Hamilton S G, Pangilinan L E, Mehmedovic Z, Yin H, Robinson P J, Roh I, Kavner A, Alexandrova A N, Tolbert S H and Kaner R B 2024 *Chem. Mater.* **36** 3233
[25] El-Atwani O, Hattar K, Hinks J A, Greaves G, Harilal S S and Hassanein A 2015 *J. Nucl. Mater.* **458** 216
[26] Mu Y C, Shen C J, Li Z, Shi S J and Xiong L 2025 *Int. J. Refract. Met. Hard Mater.* **126** 106945
[27] Rieth M, Dudarev S L, de Vicente S M G, *et al.* 2013 *J. Nucl. Mater.* **432** 482
[28] Wang L, Hong B B, Chen H Y, Qi H, Zhang J G, Hang W, Han Y X, Wang J H, Ren K and Lyu B 2025 *Powder Technol.* **455** 120758
[29] Qin C L, Liu J D, Ma S Y, Du J G, Jiang G and Zhao L 2024 *Intermetallics* **172** 108384
[30] Kalita D, Józwik I, Kurpaska L, Zhang Y, Mulewska K, Chrominski W, O'Connell J, Ge Y, Boldman W L, Rack P D, Wang Y, Weber W J and Jagielski J 2023 *Nucl. Mater. Energy* **37** 101513
[31] El-Atwani O, Li N, Li M, Devaraj A, Baldwin J K S, Schneider M M, Sobieraj D, Wróbel J S, Nguyen-Manh D, Maloy S A and Martinez E 2019 *Sci. Adv.* **5** eaav2002
[32] Shi Y Z, Jiang Z Y, Xia T J, Zhang W J, Yang P S, Ren X Y, Wang M Q, Liang L S, Cao X Z and Zhu K G 2023 *J. Nucl. Mater.* **578** 154335
[33] Cui M H, Gao N, Wang D, Gao X and Wang Z G 2019 *Nucl. Instrum. Methods Phys. Res., Sect. B* **460** 60
[34] Kresse G and Furthmüller J 1996 *Comput. Mater. Sci.* **6** 15
[35] Kresse G and Furthmüller J 1996 *Phys. Rev. B* **54** 11169
[36] Blochl P E 1994 *Phys. Rev. B* **50** 17953
[37] Perdew J P, Burke K and Ernzerhof M 1996 *Phys. Rev. Lett.* **77** 3865
[38] Featherston F H and Neighbours J R 1963 *Phys. Rev.* **130** 1324
[39] Kong X S, Song C, Chen L, Xie Z M, Liu C S and Hou J 2022 *Tungsten* **4** 231
[40] Zhang N N, Zhang Y J, Yang Y, Zhang P, Hu Z Y and Ge C C 2017 *Eur. Phys. J. B* **90** 101
[41] Zhou H B, Li Y H and Lu G H 2016 *Comput. Mater. Sci.* **112** 487
[42] Zhang N N, Zhang Y J, Yang Y, Zhang P and Ge C C 2019 *Phys. Lett. A* **383** 2777
[43] You Y W, Hou J, Sun J J, Kong X S, Wu X B, Liu C S and Chen J L 2018 *J. Nucl. Mater.* **499** 1
[44] Henkelman G, Uberuaga B P and Jónsson H 2000 *J. Chem. Phys.* **113** 9901
[45] Wang Q Q, Kong X G, Yu Y, Xin T Y, Pan R J and Wu L 2023 *J. Nucl. Mater.* **587** 154706
[46] Yang L, Liu H and Zu X 2009 *Int. J. Mod. Phys. B* **23** 2077
[47] Becquart C S and Domain C 2006 *Phys. Rev. Lett.* **97** 196402
[48] Kawabe T 2019 *Sci. Rep.* **9** 14993
[49] Su Z, Yang J, Zhou X, Li J, Zhang P, Zhang C, Shi T, Jin K, Sun Y, Wu L, Wu X, Ma E and Lu C 2025 *J. Mater. Sci. Technol.* **227** 142
[50] Zhao S J 2021 *J. Am. Ceram. Soc.* **104** 1874
[51] González C and Iglesias R 2014 *J. Mater. Sci.* **49** 8127
[52] Roy A, Singh P, Balasubramanian G and Johnson D D 2022 *Acta Mater.* **226** 117611
[53] Wang X K, Yang Q K, Wu W S, Zhang W, Zhang Y, Yan D S, Gan K F, Liu B and Li Z M 2025 *Acta Mater.* **282** 120501